

Future Response of Temperature and Precipitation to Reduced Aerosol Emissions as Compared with Increased Greenhouse Gas Concentrations

JUAN C. ACOSTA NAVARRO

Department of Environmental Science and Analytical Chemistry, and Bolin Centre for Climate Research, Stockholm University, Stockholm, Sweden

ANNICA M. L. EKMAN, FRANCESCO S. R. PAUSATA, AND ANNA LEWINSCHAL

Department of Meteorology, and Bolin Centre for Climate Research, Stockholm University, Stockholm, Sweden

VIDYA VARMA

National Institute of Water and Atmospheric Research, Wellington, New Zealand

ØYVIND SELAND, MICHAEL GAUSS, TROND IVERSEN, AND ALF KIRKEVÅG

Norwegian Meteorological Institute, Oslo, Norway

ILONA RIIPINEN AND HANS CHRISTEN HANSSON

Department of Environmental Science and Analytical Chemistry, and Bolin Centre for Climate Research, Stockholm University, Stockholm, Sweden

(Manuscript received 21 June 2016, in final form 14 October 2016)

ABSTRACT

Experiments with a climate model (NorESM1) were performed to isolate the effects of aerosol particles and greenhouse gases on surface temperature and precipitation in simulations of future climate. The simulations show that by 2025–49 a reduction of aerosol emissions from fossil fuels following a maximum technically feasible reduction (MFR) scenario could lead to a global and Arctic warming of 0.26 and 0.84 K, respectively, as compared with a simulation with fixed aerosol emissions at the level of 2005. If fossil fuel emissions of aerosols follow a current legislation emissions (CLE) scenario, the NorESM1 model simulations yield a nonsignificant change in global and Arctic average surface temperature as compared with aerosol emissions fixed at year 2005. The corresponding greenhouse gas effect following the representative concentration pathway 4.5 (RCP4.5) emission scenario leads to a global and Arctic warming of 0.35 and 0.94 K, respectively. The model yields a marked annual average northward shift in the intertropical convergence zone with decreasing aerosol emissions and subsequent warming of the Northern Hemisphere. The shift is most pronounced in the MFR scenario but also visible in the CLE scenario. The modeled temperature response to a change in greenhouse gas concentrations is relatively symmetric between the hemispheres, and there is no marked shift in the annual average position of the intertropical convergence zone. The strong reduction in aerosol emissions in the MFR scenario also leads to a net southward cross-hemispheric energy transport anomaly both in the atmosphere and ocean, and enhanced monsoon circulation in Southeast Asia and East Asia causing an increase in precipitation over a large part of this region.

 Denotes Open Access content.

 Supplemental information related to this paper is available at the Journals Online website: <http://dx.doi.org/10.1175/JCLI-D-16-0466.s1>.



This article is licensed under a [Creative Commons Attribution 4.0 license](https://creativecommons.org/licenses/by/4.0/).

Corresponding author e-mail: Juan C. Acosta Navarro, juan-camilo.acosta@aces.su.se

DOI: 10.1175/JCLI-D-16-0466.1

© 2017 American Meteorological Society

1. Introduction

In the past century, human activities have altered the chemical composition and physical properties of the atmosphere. The Intergovernmental Panel on Climate Change (Boucher et al. 2013) estimated that emissions of anthropogenic aerosol particles and their precursors have caused a net cooling of the global climate during the industrial period, partly offsetting the warming caused by greenhouse gases. However, the uncertainty in the aerosol forcing is large: estimates of total preindustrial to present-day aerosol forcing range from being the second largest anthropogenic effect to a minor perturbation of the global climate. Satellite-based observations suggest the former estimate to be more likely, giving a total effective radiative forcing from aerosols between -0.95 and -0.45 W m^{-2} (Boucher et al. 2013).

Most countries with developed industries started emission reductions in the 1980s as a response to acid rain. One of the main aerosol precursors, sulfur dioxide (SO_2), has been mostly emitted in the Northern Hemisphere (NH). NH SO_2 emissions represented about 90% and 80% of the global anthropogenic SO_2 emissions in 1940 and 2005, respectively (Smith et al. 2011). In contrast to the steady growth of carbon dioxide (CO_2) concentrations during the last century, global average SO_2 emissions peaked in the 1980s (Smith et al. 2011) and had decreased by approximately 12% in 2005. Current technology would allow for a further reduction of present-day global fossil fuel aerosol emissions by 70%–80% (Klimont et al. 2016; Z. Klimont et al. 2016, unpublished manuscript). However, future anthropogenic aerosol emission reductions largely rely on the success of air pollution control policies. Apart from few recent studies (Stohl et al. 2015; Baker et al. 2015; Westervelt et al. 2015; Pausata et al. 2015), relatively little is known about how these emission reductions will influence the climate. It is expected that as the cooling effect of aerosol particles is diminished, the warming caused by greenhouse gases will be more evident (e.g., Acosta Navarro et al. 2016).

The radiative forcing at the top of the atmosphere (TOA) caused by atmospheric aerosols is spatially heterogeneous and pronounced in regions close to the emission sources. This is due to the relatively short atmospheric residence times (less than a week in the atmospheric boundary layer) of tropospheric aerosol particles as compared with long-lived greenhouse gases. Most anthropogenic aerosol particle emission reductions have taken place in the NH, leading to a meridional asymmetry in the implied resulting forcing (Bellouin et al. 2011). The temperature response, however, is not necessarily collocated with the forcing (Palmer 1999; Boer and Yu 2003; Shindell and Faluvegi 2009; Ming and Ramaswamy 2011;

Lewinschal et al. 2013). Based on model experiments, Acosta Navarro et al. (2016) found that the unmasking effect of reduced SO_2 emissions in Europe could have explained about half of the Arctic warming trend between 1980 and 2005. Najafi et al. (2015) estimated that about 60% of the twentieth-century Arctic warming has been masked because of a gradual increase in emissions of aerosols and precursors. Similar findings were reported by Yang et al. (2014). The spatially uneven distribution of the aerosol forcing may also induce changes in tropical precipitation caused by shifts in the mean location of the intertropical convergence zone (ITCZ) (Rotstayn and Lohmann 2002; Kristjánsson et al. 2005; Kang et al. 2008; Hwang et al. 2013; Seo et al. 2014; Ridley et al. 2015). A meridional asymmetry in the forcing may cause changes in the meridional gradient of sea surface temperature (SST) that may further lead to changes in the meridional atmospheric energy transport (Hill et al. 2015). Previous studies have shown a tight coupling between shifts in the mean zonal position of the ITCZ and the cross-hemisphere atmospheric energy transport (Kang et al. 2008; Seo et al. 2014). Using numerical model simulations in aquaplanet mode, it has been found that a midlatitude surface heating in the NH causes stronger northward migration of the ITCZ than a NH tropical or subtropical surface heating of similar magnitude due to larger radiative feedbacks at the midlatitudes than in the tropics (Seo et al. 2014). Moreover, the stronger the midlatitude surface heating in the NH is, the stronger the northward migration of the ITCZ (Kang et al. 2008).

In this study we investigate the potential climate impacts of future air quality policies by studying the links between aerosol emissions, energy budget, temperature, and precipitation. We use the coupled ocean–atmosphere circulation model called NorESM1 (Bentsen et al. 2013; Iversen et al. 2013) with an explicit representation of aerosol life cycle and microphysics (Kirkevåg et al. 2013) to simulate the transient climate response to two different near-future aerosol emission scenarios corresponding to different air quality policies. We compare the surface temperature and precipitation responses caused by the aerosol emission changes to those of well-mixed greenhouse gases. To better understand the mechanisms linking aerosol changes (dominating at midlatitudes) to Arctic temperature and tropical precipitation changes, we further investigate the changes in meridional energy transport as simulated by the model.

2. Methods

a. Model description

The Norwegian Earth System Model, version 1 (NorESM1), is a fully coupled ocean–atmosphere general

circulation model. The atmospheric component has a resolution of 1.9° latitude by 2.5° longitude in the horizontal and 26 vertical levels, while the isopycnic coordinate ocean model has a grid with 1° resolution along the equator. An explicit aerosol microphysical life cycle representation (condensation, coagulation, cloud processing, new particle formation, and wet and dry deposition) for nucleation, with Aitken, accumulation, and coarse size modes of sulfate, black carbon, organic matter, mineral dust, and sea spray aerosol species, is included in the model. Hygroscopic swelling of particles is accounted for and used in the aerosol optics calculations (Kirkevåg et al. 2013). Transport of aerosol is done by the finite-volume dynamical core of the model. Aerosol species can be internally or externally mixed and activate to cloud droplets following the Köhler theory for a multicomponent aerosol population. The activation depends on the aerosol solubility, size distribution, and maximum supersaturation of the ascending air parcel (Abdul-Razzak and Ghan 2000). Aerosol–radiation and cloud–radiation interactions affect the meteorology interactively. The radiative effects of aerosol particles are estimated every time step through precalculated optics (for the direct effect) and dry size parameters (for activation and indirect effects) from lookup tables created offline from a sectional microphysics model. A full description of the atmospheric and microphysical processes in NorESM1 is found in Kirkevåg et al. (2013) and references therein. One major advantage of including explicit aerosol physics is that climate feedbacks are considered (e.g., between aerosols and clouds and precipitation).

b. Model experiments

We simulate four different emission scenarios (Table 1) and for each scenario we carry out three ensemble simulations. Each ensemble member simulation was started from year 1990 conditions from different historical CMIP5 simulations. We investigated the climate effects of two radically different fossil fuel aerosol and aerosol precursor emission scenarios developed by the International Institute for Applied Systems Analysis (IIASA) within the Evaluating the Climate and Air Quality Impacts of Short-Lived Pollutants (ECLIPSE) and Pan-European Gas–Aerosols Climate Interaction Study (PEGASOS) projects (Klimont et al. 2016; Z. Klimont et al. 2016, unpublished manuscript): the current legislation emissions (CLE) and the maximum technically feasible reduction (MFR) scenarios. The CLE scenario assumes that all existing and planned legislation on emissions is fully implemented, perfectly enforced, and delivers the expected emission reductions. On the other hand, it does not assume any further developments of such legislation in the future. The MFR scenario assumes unconditional implementation of all

TABLE 1. Description of transient simulations. Each ensemble is composed of three runs initialized at 1990 with different initial conditions from historical NorESM1 runs. Greenhouse gas concentrations are taken from Taylor et al. (2012) following the RCP4.5 scenario. CLE aerosol and precursor emissions are from Lamarque et al. (2010) between 1990 and 2000 and from IIASA ECLIPSE V4 CLE after 2005, with a linear interpolation between 2000 and 2005. MFR scenario aerosol and precursor emissions are identical to CLE before 2015. After 2016 they follow IIASA ECLIPSE V4 MFR.

Simulation ensemble	Period	Greenhouse gas scenario	Primary aerosol and precursor emissions from fossil fuels
RCP4.5_CLE	1990–2050	CMIP5, RCP4.5	CMIP5, CLE
RCP4.5_2005	1990–2050	CMIP5, RCP4.5	CMIP5, Fixed 2005
2005_CLE	1990–2050	CMIP5, fixed 2005	CMIP5, CLE
RCP4.5_MFR	1990–2050	CMIP5, RCP4.5	CMIP5, MFR

currently available emission reduction technologies, but no nontechnical measures (e.g., changes in population behavior) that would improve resource efficiency. In the CLE scenario, global average fossil fuel SO_2 , black carbon (BC), and organic carbon (OC) emissions decrease by approximately 5%, 15%, and 20%, respectively, between 2010 and 2050. The stringent reduction policies assumed in the MFR scenario yield a reduction of 73%, 75%, and 86%, respectively for SO_2 , BC, and OC. The emissions of aerosol and precursors by 2050 in the RCP scenarios (Taylor et al. 2012) used for the climate projections (not included in this study) typically fall between the values of MFR and CLE scenarios presented in this article. For example, between 2005 and 2050, representative concentration pathway 4.5 (RCP4.5) scenario SO_2 , BC, and OC emissions decrease by about 60%, 25%, and 25%, respectively, whereas in the representative concentration pathway 8.5 (RCP8.5) scenario SO_2 , BC, and OC emissions decrease by about 60%, 35%, and 15%, respectively. In the CLE scenario, European and North American emissions follow the current decreasing trend in the future, whereas East Asian emissions (led by China) peak in about 2020 to return to present-day levels in 2030 and continue decreasing afterward. South Asian emissions (led by India) continue to increase driven by economic development and low control measures. Under the MFR scenario, all nations reduce their emissions after 2015 assuming a full implementation of present-day emission control technologies gradually until 2030. For further details on the construction of the emission scenarios and technical aspects, see Klimont et al. (2016) or the IIASA web page http://www.iiasa.ac.at/web/home/research/researchPrograms/air/Global_emissions.html. For

TABLE 2. Description of the 25-yr ensemble mean differences (between two scenarios) used in the analysis.

Name	Calculation	Period	Effect detection
GHG	RCP4.5_CLE minus 2005_CLE	2025–49	GHG (RCP4.5 minus present)
CLE-2005	RCP4.5_CLE minus RCP4.5_2005	2025–49	Aerosol (CLE minus present)
MFR-2005	RCP4.5_MFR minus RCP4.5_2005	2025–49	Aerosol (MFR minus present)

greenhouse gas concentrations, the RCP4.5 scenario was applied (Taylor et al. 2012). Note that air quality control measures affect methane emissions and tropospheric ozone production and vary between the CLE and MFR scenarios. This study is focused only on the aerosol effects on climate of future air quality controls, and the comparison between the climate response of an aerosol-induced spatially inhomogeneous radiative flux perturbation with a more homogeneous greenhouse gas-induced radiative flux perturbation.

The four scenarios investigated in this study are the following (Table 1): RCP4.5_CLE represents the evolution of climate following the RCP4.5 scenario for greenhouse gas concentrations and CLE scenario for fossil fuel aerosol emissions, respectively. RCP4.5_2005 and 2005_CLE are similar to RCP4.5_CLE, but in RCP4.5_2005 fossil fuel aerosol emissions were kept at 2005 levels, whereas in 2005_CLE, greenhouse gas concentrations were fixed at 2005 levels. RCP4.5_MFR represents the evolution of climate following the RCP4.5 scenario for greenhouse gas concentrations and MFR scenario for fossil fuel aerosol emissions. All simulations span the time period from 1990 to 2050. Assuming that the climate effects of aerosol and greenhouse gases are linear (Kirkevåg et al. 2008), the greenhouse gas (GHG) effect on climate is calculated as the difference between scenarios RCP4.5_CLE and 2005_CLE (GHG case in Table 2) for the last 25 years of simulation. The effect of two different aerosol emission policies on climate is explored by taking the differences between scenarios RCP4.5_CLE and RCP4.5_2005, and between RCP4.5_MFR and RCP4.5_2005, for the last 25 years of simulation (CLE-2005 and MFR-2005 in Table 2, respectively).

c. Data analysis: Energy and mass transport calculations

To gain insight into the mechanisms behind the climate response to aerosol and greenhouse gas emissions, we investigated the changes in the energy transport and distribution within the Earth system caused by the anomalies outlined in Table 2. Below we summarize the equations used in this analysis.

Local energy conservation is expressed as (Trenberth 1997; Fasullo and Trenberth 2008a,b)

$$\frac{\partial \bar{A}}{\partial t} + \bar{\nabla} \cdot \mathbf{F}_A = \bar{Q}^{\text{TOA}} - \bar{Q}^{\text{Surf}}. \quad (1)$$

The overbars denote temporal means, A is the vertically integrated atmospheric energy content per unit surface area (J m^{-2}), \mathbf{F}_A is the vertically integrated horizontal energy transport vector per unit length (W m^{-2}), and Q^{TOA} and Q^{Surf} are the net downward energy fluxes (W m^{-2}) at the top of the atmosphere and at the surface, respectively. Over a sufficiently long period, the first term in Eq. (1) on the left-hand side is much smaller than the remaining terms and can be neglected. Using this steady-state assumption, taking only the meridional component of the transport vector and discretizing the integrals to match the atmospheric model grid yields

$$\overline{F_A(\phi)} = \overline{F_{A_n}} = a^2 \sum_{i=1}^{144} \sum_{j=1}^n (\overline{Q_{ij}^{\text{TOA}}} - \overline{Q_{ij}^{\text{Surf}}}) \cos(\phi_j) \Delta\phi_j \Delta\theta_i, \quad (2)$$

where $F_A(\phi)$ is the zonally integrated meridional energy transport (watts) in the atmospheric column as a function of latitude, a is the mean radius of Earth (meters), and θ and ϕ are the longitude and latitude coordinates, respectively. Indices i and j represent the discrete running indices for θ and ϕ , respectively. The index i runs over the whole latitude band (with 144 longitudes), while the index j runs from the South Pole to the specific latitude ϕ , represented by the index n .

The product of the specific humidity q (kg kg^{-1}) and the meridional component of the wind velocity v (m s^{-1}) is diagnosed directly in the model with a temporal resolution of half an hour. This product is summed vertically and zonally and averaged over the desired period to get the latent heat meridional transport (watts):

$$\overline{F_{\text{Latent}}}(\phi) = \overline{F_{\text{Latent}_n}} = \frac{L_v a \cos(\phi)}{g} \sum_{i=1}^{144} \sum_{k=1}^{26} \overline{q_{i,n,k} v_{i,n,k} \Delta p_{i,n,k} \Delta\theta_i}, \quad (3)$$

where g is the mean acceleration by gravity at Earth's surface (m s^{-2}), L_v is the latent heat of vaporization of water at standard conditions (J kg^{-1}), and p is the pressure coordinate (pascal) and k the index corresponding to it. The indices i and k run over the whole

latitude band and vertical extent of the atmosphere, respectively.

Neglecting the kinetic energy related to winds (see, e.g., Trenberth and Stepaniak 2003), the total meridional atmospheric energy transport is approximately equal to the moist static energy transport. The dry static energy transport F_{DS} is thus expressed as

$$\overline{F_{DS}(\phi)} = \overline{F_A(\phi)} - \overline{F_{Latent}(\phi)}. \quad (4)$$

Oceanic energy transport $F_O(\phi)$ is diagnosed directly in the ocean model with a temporal resolution of half an hour as

$$\begin{aligned} \overline{F_O(\phi)} &= \overline{F_{O_n}} \\ &= C_w a \cos(\phi) \sum_{i=1}^{320} \sum_{k=1}^{53} \overline{T_{i,n,k} \rho_{i,n,k} v_{i,n,k} \Delta z_{i,n,k} \Delta \theta_i}, \end{aligned} \quad (5)$$

where C_w is the heat capacity of water ($\text{JK}^{-1} \text{kg}^{-1}$), T is the water temperature (kelvin), z is the depth (meters), and ρ is the water mass density (kg m^{-3}). The indices for longitude i , latitude j , and depth k in the ocean model are from 1 to 320, 384, and 53 layers, respectively.

The net energy transport in the ocean–atmosphere system is therefore

$$\overline{F_{Sys}(\phi)} = \overline{F_A(\phi)} + \overline{F_O(\phi)}. \quad (6)$$

The zonal mean mass meridional streamfunction Ψ (kg s^{-1}) is calculated as (Hill et al. 2015)

$$\overline{\Psi(\phi, p)} = \overline{\Psi_{n,l}} = \frac{2\pi a \cos(\phi)}{g} \sum_{k=1}^l \overline{[v_{n,k}] \Delta p_k}, \quad (7)$$

where $[v_{j,k}] = (1/144) \sum_{i=1}^{144} v_{i,j,k}$.

Analogously, the mean meridional circulation component of the energy transport is estimated as

$$\overline{F_{Merid}(\phi)} = \frac{2\pi a \cos(\phi)}{g} \sum_{k=1}^{26} \overline{[e_{n,k}] [v_{n,k}] \Delta p_k}, \quad (8)$$

where $[e_{j,k}] = (1/144) \sum_{i=1}^{144} C_p T_{i,j,k} + L_v q_{i,j,k} + g z_{i,j,k}$, and it represents the zonally averaged moist static energy per unit mass. Also, C_p is the heat capacity of dry air at constant pressure ($\text{JK}^{-1} \text{kg}^{-1}$), and z is the geopotential height.

Approximating the Clausius–Clapeyron relation for water, the change in q scales linearly to small changes in surface temperature. This gives the approximate thermodynamic contribution to the latent heat transport as a function of latitude:

$$\frac{\delta \overline{F_{Latent}^{Therm}(\phi)}}{\overline{F_{Latent}^{Therm}(\phi)}} = \alpha \overline{\delta T(\phi)}, \quad (9)$$

where $\alpha = 0.07 \text{ K}^{-1}$ is the scaling constant derived from the latent heat of evaporation for water (Held and Soden 2006). (Note that all values in Figs. 7 and 8 are calculated from only two of the three ensemble simulations due to a lack of ocean data availability in one of the ensemble simulations.)

3. Results and discussion

a. Spatial distributions of aerosol burden changes

To better understand the simulated temperature and precipitation responses to future GHG and different aerosol emission scenarios, we first examine the changes in the spatial pattern of aerosol burden for each case (Fig. 1). The current legislation emissions compared to 2005 emissions (CLE-2005) shows a decrease of sulfate, OC, and BC aerosol burden in North America, Europe, and East Asia, whereas over India the sulfate and BC column burden increase while OC decreases (Figs. 1a,c,e). The differences in simulations following the maximum technically feasible reduction scenario versus 2005 emissions (MFR-2005) show larger sulfate, BC, and OC column burden reductions over all regions (Figs. 1b,d,f). Overall, the changes in aerosol burden in both CLE-2005 and MFR-2005 are much larger over the NH than the SH, especially for sulfate, and as expected, MFR-2005 shows a larger column burden reduction over midlatitudes than CLE-2005. Both anthropogenic aerosol emissions scenarios show that South and East Asia are important regions when it comes to future aerosol burden changes and possibly the associated climate consequences.

b. Top-of-atmosphere energy budget response

The budget of modeled differences in TOA energy caused by different aerosol versus greenhouse gas forcing is displayed in Fig. 2. The net difference in the annually averaged TOA energy flux (incoming minus outgoing) for a well-mixed greenhouse gas change is relatively evenly distributed across the globe as compared with the cases with varying aerosol emissions (Fig. 2d). The net global change of the downward energy at TOA in the GHG case is 0.42 W m^{-2} (Table 3). In both CLE-2005 and MFR-2005 there is an increase in net downward energy at the TOA at midlatitudes, being stronger in MFR-2005 than in CLE-2005. The CLE-2005 case shows a decrease of the net downward energy at the TOA over India caused by the increase in sulfate aerosol burden, which dominates over the increase in net downward energy at the TOA caused by the increase of BC and decrease of OC aerosol burden over the same region. The negative TOA energy changes over India in CLE-2005 compensate most of the net increase of energy

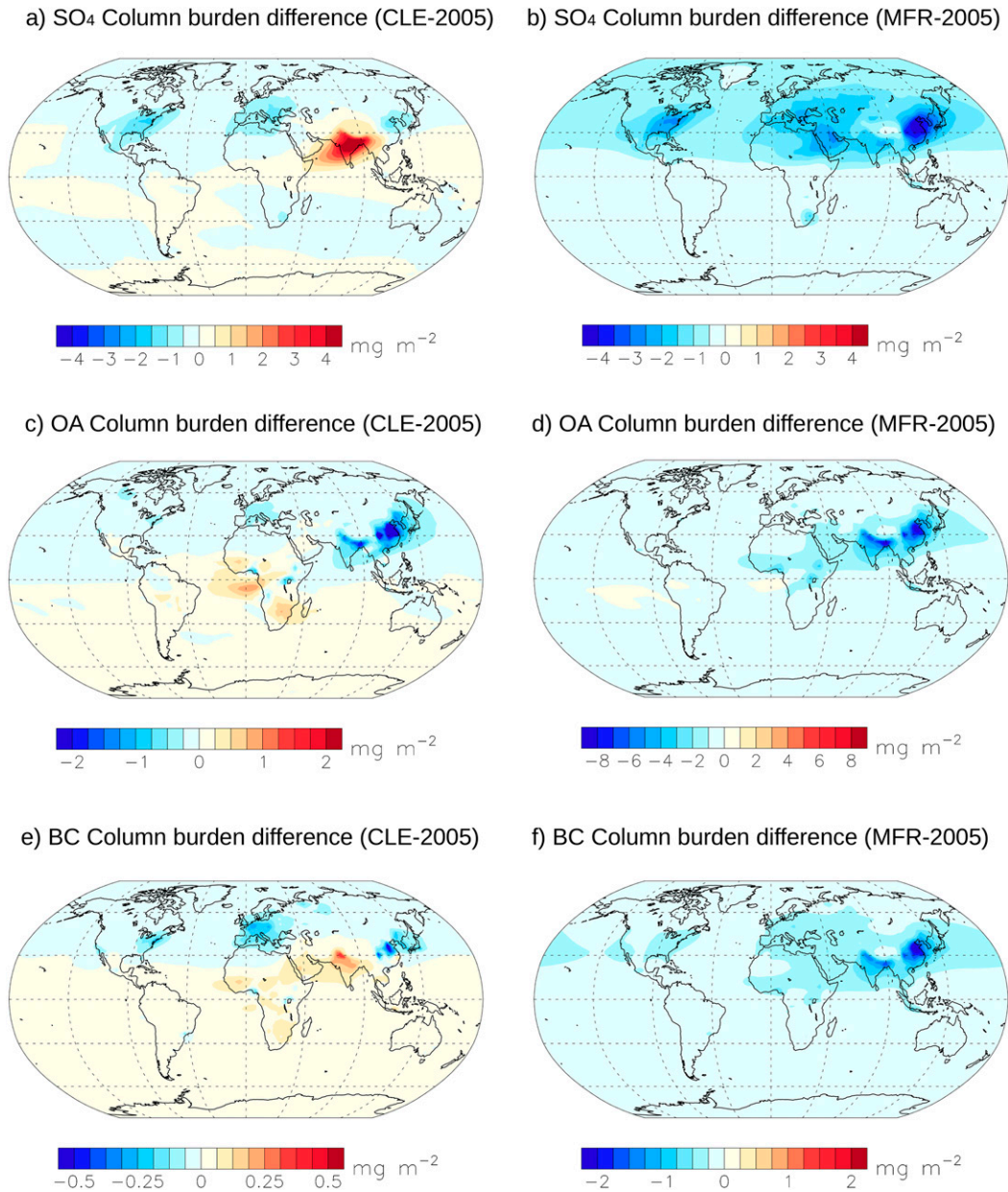


FIG. 1. Aerosol column burden changes in CLE-2005 and MFR-2005. Difference (CLE-2005) in the mean 2025–49 column burden of (a) sulfate (SO_4), (c) OC, and (e) BC aerosol. Difference (MFR-2005) in the mean 2025–49 column burden of (b) sulfate, (d) OC, and (f) BC aerosol.

caused by the aerosol burden decrease over midlatitudes (North America, Europe, and East Asia). The net global change of the downward energy at the TOA in CLE-2005 is small (0.05 W m^{-2} ; Table 3). The changes in net TOA energy over India are positive in MFR-2005 and lower in magnitude compared to CLE-2005, while the midlatitude changes are stronger because of larger aerosol emission reductions over North America, Europe, and East Asia. The net global change in the downward energy flux at the

TOA in MFR-2005 is 0.31 W m^{-2} (Table 3). The sulfate and BC aerosol reduction patterns in Figs. 1a,b and 1e,f, are similar to the positive TOA changes in Figs. 2b,c over most regions. The radiative effect caused by the removal of sulfate aerosol dominates over that of the removal of BC showing that in NorESM1 sulfate is the dominant anthropogenic aerosol climate forcing agent. There is a TOA radiative budget change in CLE-2005 and MFR-2005 in the East Asian outflow region of the North

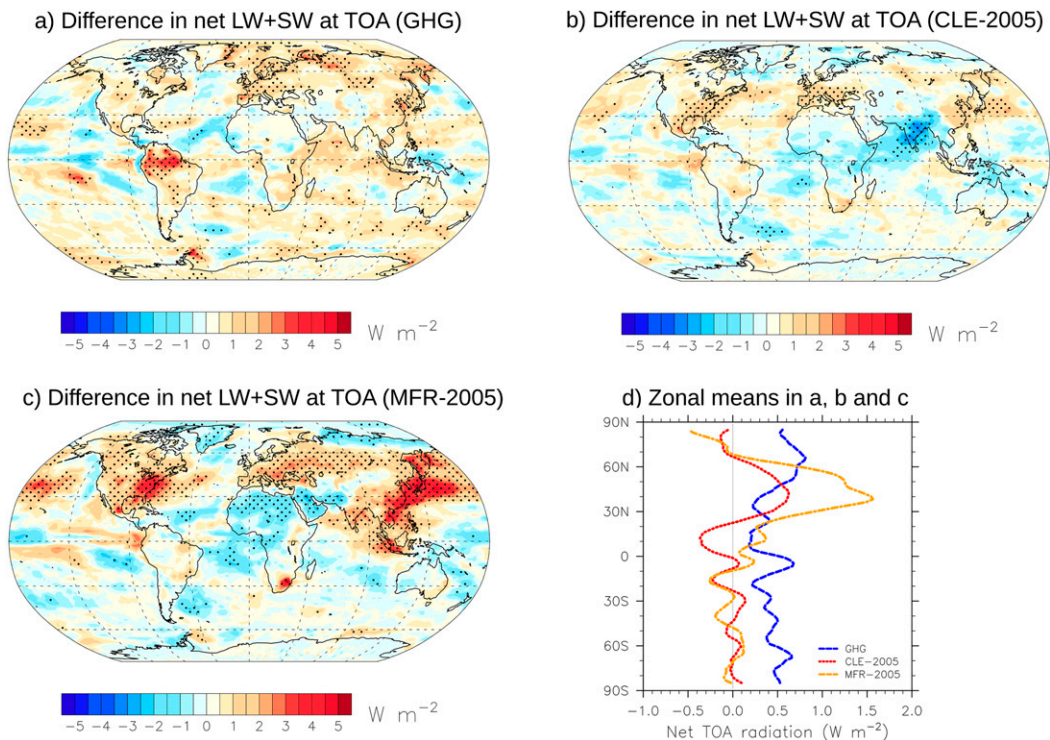


FIG. 2. TOA radiation budget changes ($\Delta\overline{Q}^{\text{TOA}}$). Mean 2025–49 difference in net downward TOA longwave plus shortwave radiation for ensemble runs for (a) GHG, (b) CLE-2005, and (c) MFR-2005 cases. (d) Zonal means of the results displayed in (a)–(c). The black dots in (a)–(c) indicate statistical significant differences in the 25-yr mean values at a 95% confidence level, estimated with the Student's t test.

Pacific, which is much stronger in MFR-2005 than CLE-2005. Additionally, the net TOA radiative flux difference is negative and statistically significant over the Sahara, the Arabian Peninsula, and north of the Persian Gulf for MFR-2005, despite the reduction of reflective aerosol burden (mostly sulfate) over these regions. The reason is the high albedo of the underlying surface.

A formal quantification of the radiative forcings and associated feedbacks is out of scope of this study; however, the decomposition of the net TOA radiative fluxes into clear-sky and cloudy-sky components allows for a qualitative interpretation and identification of positive and negative feedbacks in the simulations with increasing greenhouse gases (GHG case) and decreasing aerosol emissions (MFR-2005). The positive TOA radiative fluxes caused by the GHG increase are damped by negative cloud feedbacks over ocean regions and enhanced by positive cloud feedbacks over land regions (Figs. S1a,c and S2a in the supplemental material). The net global cloud feedback is negative in the GHG case (Fig. S1c). The clear-sky response in the GHG case also indicates that the positive water vapor and high-latitude surface albedo feedbacks are main drivers of the net energy gain at the TOA (Figs. S1a and S2a). In MFR-2005,

clouds generally reinforce the clear-sky positive TOA radiative flux induced by lower aerosol particle loadings (Figs. S1b,d and S2c). This feature is related to the aerosol indirect effects. The positive water vapor and high-latitude surface albedo feedbacks are also evident in the NH in MFR-2005 (Fig. S1b) where temperature changes are the strongest.

c. Surface temperature response

The evolution of global surface temperature in RCP4.5_2005 is similar to RCP4.5_CLE (Fig. 3), both having a warming trend of about $0.15\text{ K decade}^{-1}$ between 2010 and 2050. This is the same as the observed trend (Hansen et al. 2010) during 1970–2010. The simulation for 2005_CLE shows a slowdown of the warming around 2030, and the system approaches an equilibrium which is about 0.2 K warmer than in years 2001–10. In RCP4.5_MFR there is a strong warming (about 0.3 K decade^{-1}) during 2015–30 when aerosol emissions are reduced, whereas the trend after 2030 is similar in both RCP4.5_MFR and RCP4.5_CLE. At the end of the simulation (2040–49), the global mean surface temperature is about 0.3 K warmer in RCP4.5_MFR than in RCP4.5_CLE. It is worth noting that beyond 2050 the

TABLE 3. Estimated time-averaged (2024–49) global and hemispheric TOA energy flux difference, global, hemispheric, and Arctic (65°–90°N) temperature difference, Arctic amplification coefficient, global and land precipitation (precip) difference, and northward shift of the ITCZ for the three cases presented in Table 2.

Variable	GHG	CLE-2005	MFR-2005
TOA energy flux (W m^{-2})			
Δ shortwave	0.25	0.14	0.68
Δ longwave	0.17	−0.09	−0.37
Δ net	0.42	0.05	0.31
Δ net NH	0.39	0.11	0.64
Δ net SH	0.45	0.00	−0.02
Surface temperature (K)			
Δ global	0.35	0.03	0.26
Δ NH	0.46	0.07	0.43
Δ SH	0.24	−0.02	0.09
Δ Arctic	0.94	0.03	0.84
Δ Arctic/ Δ global	2.7	1.0	3.2
Total precipitation (mm yr^{-1})			
Δ precip (65°–90°N)	11.8 (3.1%)	0.4 (0.0%)	16.5 (4.3%)
Δ precip (35°–65°N)	4.7 (0.5%)	4.4 (0.5%)	16.0 (1.9%)
Δ precip (0°–35°N)	10.6 (0.9%)	16.1 (1.3%)	35.3 (3.0%)
Δ precip (35°S–0°)	−5.0 (−0.4%)	−15.0 (−1.2%)	−16.1 (−1.3%)
Δ precip (65°–35°S)	3.6 (0.4%)	0.7 (0.0%)	4.0 (0.4%)
Δ precip (65°–90°S)	6.0 (1.7%)	−1.1 (−0.2%)	4.2 (1.2%)
Land precipitation (mm yr^{-1})			
Δ precip (65°–85°N)	7.7 (1.9%)	0.1 (0.0%)	13.7 (3.5%)
Δ precip (35°–65°N)	2.0 (0.2%)	5.2 (0.9%)	16.2 (2.9%)
Δ precip (0°–35°N)	9.1 (1.1%)	3.9 (0.5%)	17.1 (2.2%)
Δ precip (35°S–0°)	17.7 (1.6%)	−5.2 (−0.5%)	−5.0 (−0.4%)
Δ precip (55°–35°S)	2.2 (0.4%)	−3.1 (−0.6%)	−2.9 (−0.6%)
Δ precip (65°–90°S)	5.1 (2.6%)	−1.3 (−0.6%)	1.7 (0.9%)
Northward shift of ITCZ (° lat)			
Annual	0.2	0.7	1.0
June–August	1.2	0.8	1.1
December–February	−0.3	0.2	0.3

greenhouse gas effect will dominate over the aerosol effect in both scenarios. According to multimodel estimates (Taylor et al. 2012) and NorESM1 projections (Iversen et al. 2013), the temperature could increase by an additional 0.5 K between 2050 and 2100 in the RCP4.5 scenario. The Arctic temperature response to strong aerosol reductions (MFR-2005; Table 3), 0.8 K, is almost as large as the one caused by increasing greenhouse gases (GHG case; Table 3), 0.9 K. However, the ratio of Arctic to global temperature increase is higher in MFR-2005 than in the GHG case (3.2 and 2.7, respectively in Table 3). The difference in amplification factors between the MFR-2005 and GHG cases is significantly larger than zero at a 93% and 97% confidence level for the final 25-yr (2025–49) and the final 20-yr (2030–49) period of simulations, respectively.

The positive well-mixed forcing in the GHG case and the NH-dominated forcing in MFR-2005 give rather similar results north of 40°N in terms of total warming and spatial distribution, with larger warming concentrated over

the Arctic and the continents (Fig. 4 and Table 3). Over the NH, the warming is statistically significant in most locations for both the GHG and MFR-2005 cases. CLE-2005 results in much smaller changes in temperature than the GHG and MFR-2005 cases showing modest warming close to the regions where most of the aerosol reductions take place (North America, Europe, and East Asia; cf. Figs. 1a, 2b, and 4b). The asymmetry in the aerosol forcing in MFR-2005 causes a larger relative warming of the NH than the SH, where the warming is generally nonsignificant. These results are in line with Stern and Kaufmann (1999), who reported an asymmetric hemispheric temperature response to sulfate emissions in the twentieth century based on a detailed econometric time series analysis of observations. The response of sea surface temperature is fairly symmetrical between the hemispheres for the GHG case (Fig. 4e). That is not the case for MFR-2005, which shows a larger sea surface warming in the NH than in the SH. Note that the regions with the largest changes in temperature are not necessarily the same regions with

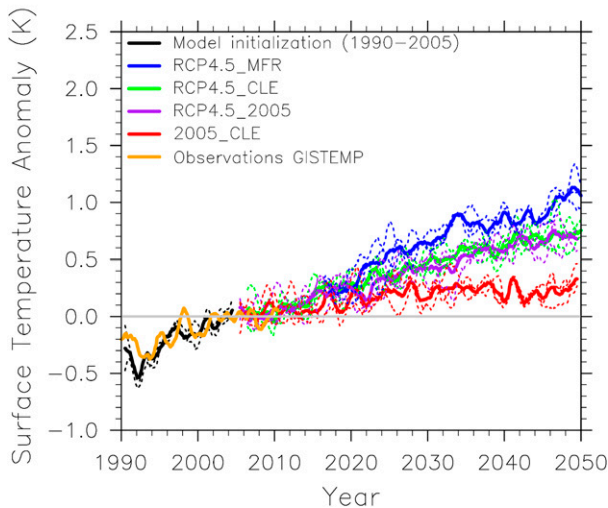


FIG. 3. Series of surface temperature evolution. Anomalies of the mean global surface temperature with respect to 2001–10 values. The yellow line displays observations from GISTEMP (Hansen et al. 2010). All dashed series represent means from individual runs and the thick solid lines are the ensemble means. All series are monthly means filtered with a 12-month running mean.

the largest anomalies in net TOA radiation. However, over some ocean regions there is an overall good spatial correlation between higher surface temperatures and positive radiative flux perturbations. This is evident in the North Pacific Ocean in MFR-2005 and CLE-2005 (Figs. 2b,c and 4b,c). Note also that the mean zonal sea surface temperature and the net positive radiative flux changes show similarities in terms of the location of the midlatitude maxima (Figs. 2d and 4e). Interestingly, this is not the case when land surface temperatures are included in the zonal mean (Fig. 4d).

In summary, our study shows similarities in the spatial distribution of the surface temperature response to aerosol and greenhouse gas emission changes, which qualitatively agrees with previous multimodel studies (Xie et al. 2013; Wang et al. 2016). However, in addition to the similarities, we here note a major difference in the differential hemispheric heating caused by the aerosol emissions reductions. Our study focuses on the difference in climatic response caused by the different forcing agents rather than the similarities.

d. Precipitation response

The spatial distribution of the total precipitation rates for the cases presented in Table 2 is shown in Fig. 5. A greenhouse gas forcing is predicted by NorESM1 to induce a narrowing of the tropical rainband with increased precipitation over the deep tropics (15°N–10°S) and drying between 15° and 30°N and between 10° and 20°S. (Figs. 5a,d). However, this seems to be valid only

over most ocean regions. Over the east Pacific and large portions of continents in the tropics, precipitation increases with increasing greenhouse gas levels outside the 15°N–10°S band. In general, the subtropics become dryer and the mid- and high latitudes wetter. This is similar to the multimodel comparison presented in Held and Soden (2006). The thermodynamic response of water vapor saturation to temperature increase most likely drives these changes (see subsection 3e).

In contrast to the greenhouse gas changes, the aerosol changes induce a more marked drying in the SH tropical band compensated by wetter conditions in the NH counterpart (Figs. 5b–e and Table 3). The magnitude of the tropical precipitation changes seems to depend on the location and strength of the aerosol-induced flux changes that are mostly concentrated in the NH. The larger warming of the NH relative to the SH yields a northward migration of the ITCZ (Table 3) that is more pronounced in MFR-2005 than in CLE-2005 because of the stronger NH warming in the MFR-2005 experiment (Fig. 4e). Interestingly, zonal mean changes in tropical precipitation (including oceans) in CLE-2005 are of similar magnitude to those in MFR-2005 and GHG cases (Fig. 5d), despite the much smaller changes in surface temperature globally and regionally (Fig. 4 and Table 3). However, MFR-2005 causes a larger increase in precipitation over the whole NH than CLE-2005. In both MFR-2005 and CLE-2005 there is a clear dipole of a wetter NH and drier SH, which is likely a result of the aerosol emission reduction at NH midlatitudes, and highlights the importance of aerosol regional forcing in inducing changes in tropical precipitation.

We further estimate the mean zonal position of the ITCZ (Table 3) by finding the latitude at which Ψ becomes zero at 500 mb [Eq. (7); 1 mb = 1 hPa]. During NH summer (winter), the relative northward displacement of the ITCZ is 1.2° (−0.3°), 0.8° (0.2°), and 1.1° (0.3°) latitude, in GHG, CLE-2005, and MFR-2005 cases, respectively. Annually, the ITCZ displacement is 0.2°, 0.7°, and 1.0° latitude, in GHG, CLE-2005, and MFR-2005 cases, respectively. An indirect estimate of the effect of changes in aerosol emissions on surface precipitation and the ITCZ during the twentieth century can be obtained by using the inverse of the results of MFR-2005, suggesting that during periods of strong increases in aerosol emissions the ITCZ would shift southward.

In MFR-2005, the Middle East is estimated to experience a large reduction in rainfall (Fig. 5), as opposed to the increase over Southeast Asia and East Asia, whereas the GHG case yields an increase in rainfall over the southern part of the Middle East (however, mostly nonsignificant). Precipitation increases significantly over

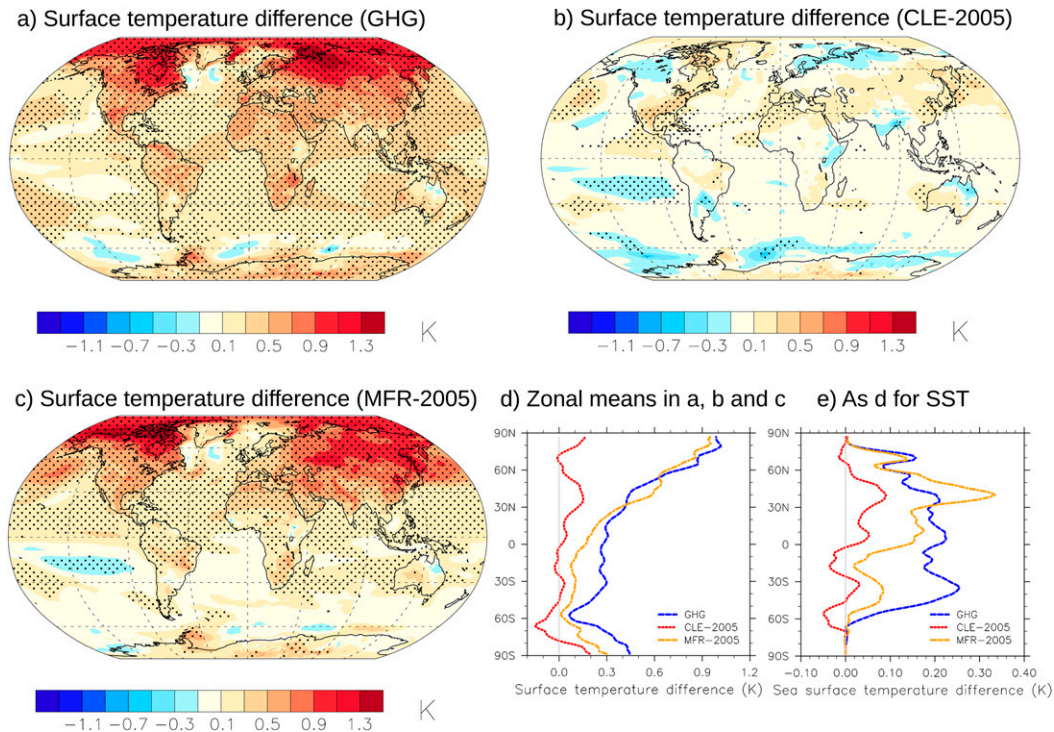


FIG. 4. Surface temperature changes. Mean 2025–49 difference in surface temperature for (a) GHG, (b) CLE-2005, and (c) MFR-2005 cases. (d) Zonal means of the results displayed in (a)–(c). (e) As in (d), but for SST. The black dots in (a)–(c) indicate statistical significant differences in the 25-yr mean values at a 95% confidence level, estimated with the Student's t test.

small areas in the eastern margin of the Sahel in the GHG case and the western margin of the Sahel in both CLE-2005 and MFR-2005. The GHG case also shows statistically significant reductions in rainfall in northwestern Mexico, Central America, and the Caribbean and Mediterranean regions. Despite the clear tropical NH–SH dipole in precipitation changes caused by CLE-2005, most of the changes over land are not statistically significant. Both GHG and MFR-2005 cases show a statistically significant increase in precipitation in many NH high-latitude locations, but the response is larger in MFR-2005 than in the GHG case. Globally, the increase in precipitation in the GHG case is 0.4%, whereas in MFR-2005 it is 0.9%, showing a larger model sensitivity of global precipitation to an aerosol-induced than a GHG-induced warming.

The monsoon rainfall in Southeast Asia and East Asia shows a strong positive response in MFR-2005, which is most likely due to an intensification of the mean monsoon circulation that drives the moisture transport from the Indian and Pacific Oceans to the continent during boreal summer (Fig. 6). This response is stronger than the responses in GHG and CLE-2005 cases. The monsoon circulation intensifies in MFR-2005 (Fig. 6d) whereas it weakens in CLE-2005 (Fig. 6c) and remains about the same in the GHG case (Fig. 6b). A diabatic heating

(potential vorticity source) at the surface over South and East Asia caused by the strong reduction of aerosol particles in MFR-2005 (Figs. 1 and 2) could be a reason why the circulation responds differently in MFR-2005 than in CLE-2005 or GHG cases. The monsoon circulation intensification (dynamic contribution) in addition to larger evaporation from warmer surrounding seas (thermodynamic contribution) are very likely responsible for the increase in precipitation in MFR-2005. Although not statistically significant, there is an increase in precipitation in the GHG case over India, which is possibly driven by the thermodynamic contribution. The drying response over the Arabian Peninsula is possibly also affected by the Asian monsoon circulation changes in MFR-2005 and contrasts with the increase in rainfall in the GHG case (Figs. 5 and 6).

e. Meridional heat transport response

Figure 7 shows the changes in $\overline{F_A(\phi)}$ decomposed into $\overline{F_{Ds}(\phi)}$, $\overline{F_{Latent}(\phi)}$, approximate thermodynamic latent $\overline{F_{Latent}^{Therm}(\phi)}$, and $\overline{F_{Merid}(\phi)}$ components for each one of the three scenario differences listed in Table 2. Both MFR-2005 and CLE-2005 yield larger changes than the GHG

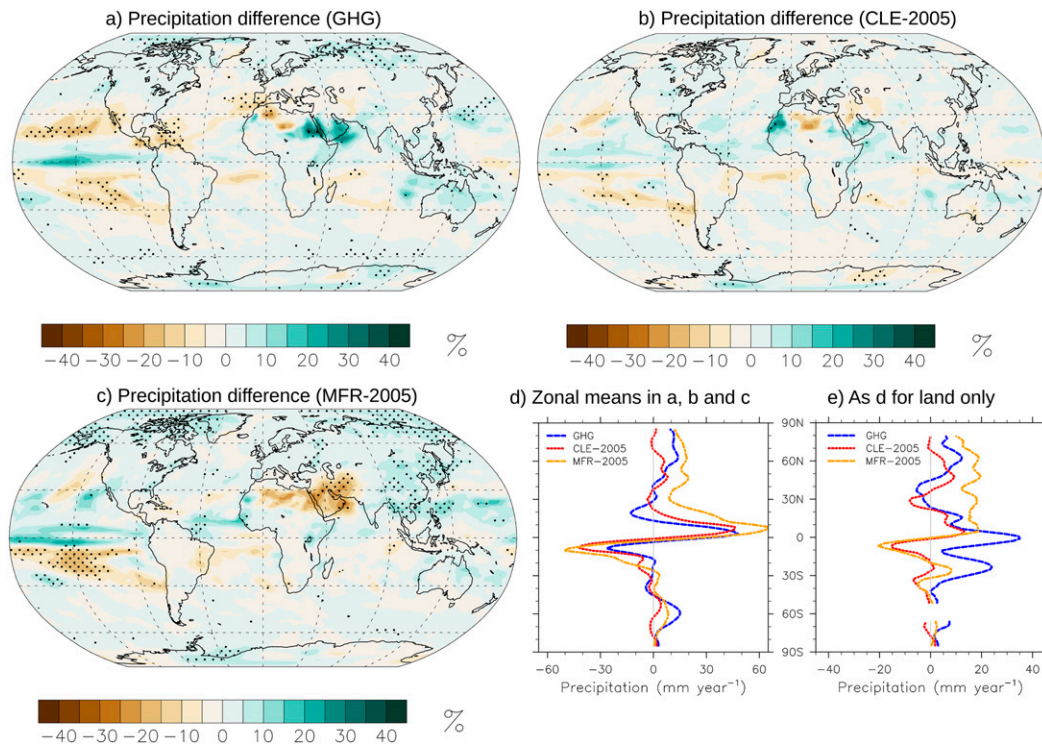


FIG. 5. Surface precipitation changes. Mean 2025–49 difference in the total precipitation rate for (a) GHG, (b) CLE-2005, and (c) MFR-2005 cases. (d) Zonal means of the results displayed in (a)–(c). (e) As in (d), but for land precipitation only. The black dots in (a)–(c) indicate statistical significant differences in the 25-yr mean values at a 95% confidence level, estimated with the Student's t test. The difference in precipitation between two simulations follows a normal distribution, justifying the use of the Student's t test.

case for the dry static, total latent, and mean meridional circulation components of energy in the tropics. The NH-dominated aerosol changes (Fig. 1) in MFR-2005 and CLE-2005 cause a stronger TOA imbalance in the NH (Fig. 2 and Table 3) than in the SH, which in turn results in a stronger change in surface temperature in the NH (Fig. 4 and Table 3). The atmosphere responds as a whole to the NH surface heating caused by the aerosol perturbations by creating an anomalous transport of energy [$\bar{F}_A(\phi)$] from NH to SH (Figs. 8b,c). The net anomalous atmospheric energy flux from NH to SH is achieved by a northward shift in the ascending branches of the Hadley cells. This in turn causes a net increase in northward cross-hemispheric latent energy transport, which is counterbalanced by a net decrease in dry static energy (Figs. 7b,c). The greenhouse gas-induced changes display a more symmetric response (Figs. 7a and 8a) but still induce stronger warming in the NH than in the SH. However, the shape in the anomaly of latent heat (Fig. 7a) indicates that the thermodynamic component (thin yellow line) partly drives the response in the GHG case, whereas the contribution from the thermodynamic component in both CLE-2005 and MFR-2005 is smaller

than the nonthermodynamic part (Figs. 7c,d). This implies that there is a smaller contribution from changes in circulation in the GHG case than in CLE-2005 and in MFR-2005, except for the southern part of the tropics, where all cases show large differences between the thermodynamic approximation and the total response. Additionally, north of about 45°N, the total atmospheric transport is negative for the GHG case and positive for CLE-2005 and MFR-2005 (Fig. 8).

Despite the fact that there is a negative TOA energy imbalance in the NH tropics and subtropics in CLE-2005 (Fig. 2d), the positive NH midlatitude TOA energy imbalance dominates, causing a warmer NH and cooler SH (Table 3), affecting tropical circulation and its associated shift of the ITCZ. This result qualitatively agrees with the findings from Seo et al. (2014), who showed that a midlatitude surface heating is more efficient at shifting the ITCZ than a tropical/subtropical surface heating of similar magnitude, when radiative feedbacks are included in the model. There is also a qualitative agreement between our results and those of Kang et al. (2008) showing that the shift in the ITCZ becomes larger with increasing surface warming at midlatitudes. The net TOA imbalance

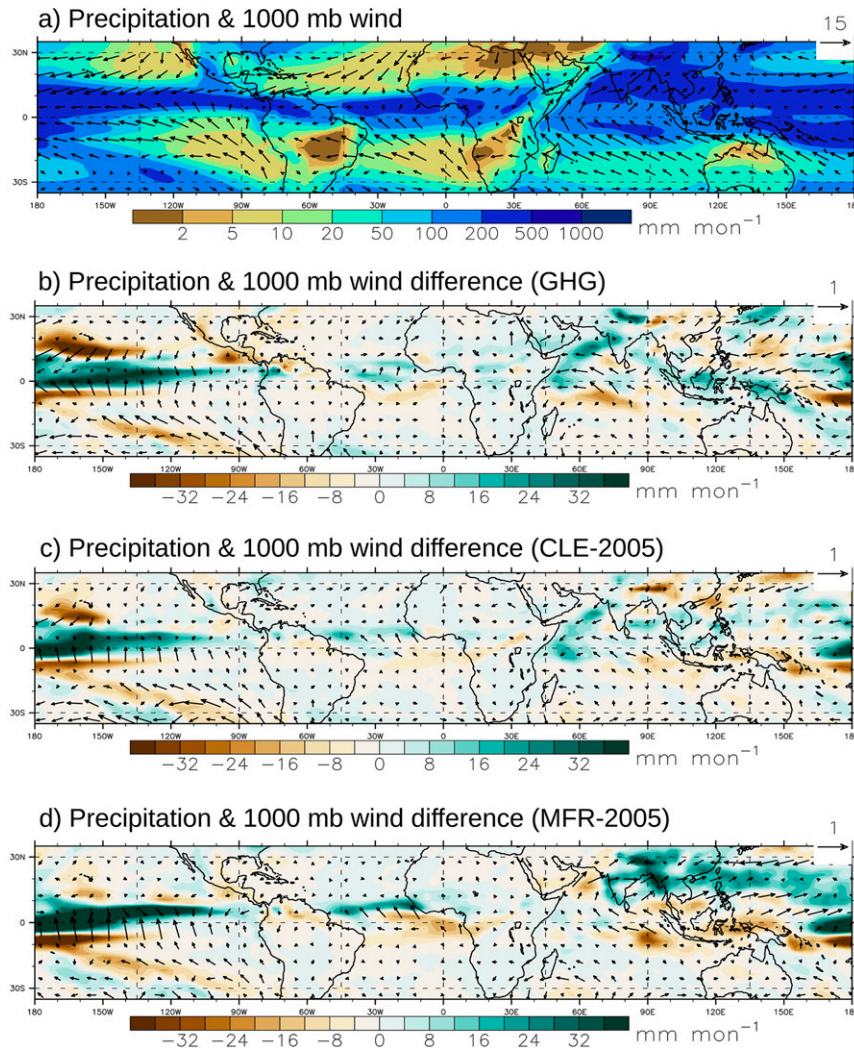


FIG. 6. Tropical surface precipitation and 1000-mb wind [June–August (JJA)]. Mean 2025–49 JJA total tropical precipitation rate and 1000-mb wind speed in (a) RCP4.5_CLE and differences in (b) GHG, (c) CLE-2005, and (d) MFR-2005 cases. The reference wind vector is 15 m s^{-1} in (a) and 1 m s^{-1} in (b)–(d).

and surface warming at NH midlatitudes in MFR-2005 are stronger than in CLE-2005, driving a larger shift in the mean position of the ITCZ and the tropical circulation response. From a policy perspective, the CLE scenario is perhaps a more feasible emission scenario than the MFR scenario, having a small global average change in aerosol emissions and surface warming, but still causing a disproportionately strong response in tropical precipitation per unit global warming, which is likely linked to the removal of aerosol particles at midlatitudes. From the human health point of view, the MFR scenario is however most likely more beneficial than the CLE scenario.

The $F_o(\phi)$ difference in GHG and CLE-2005 cases (Figs. 8a,b) compensates for most of the atmospheric

response, and keeps $\overline{F_{\text{sys}}(\phi)}$ change in the climate system between -30 and 30 TW at all latitudes. These changes are not significantly different from zero at a 95% confidence. This ocean–atmosphere coupling phenomenon is known as Bjerknes compensation (Bjerknes 1964). The compensation, however, is not evident in MFR-2005 (Fig. 8c), where both atmospheric and oceanic components reinforce each other at most latitudes. This causes a net southward energy flux at the equator of the ocean–atmosphere system that is presumably driven by the large TOA imbalance at NH midlatitudes (Fig. 2d). The climate system energy changes in MFR-2005 are significantly different from zero at 95% confidence at most latitudes in the NH. Assuming that the net TOA energy gain goes entirely into the ocean, the

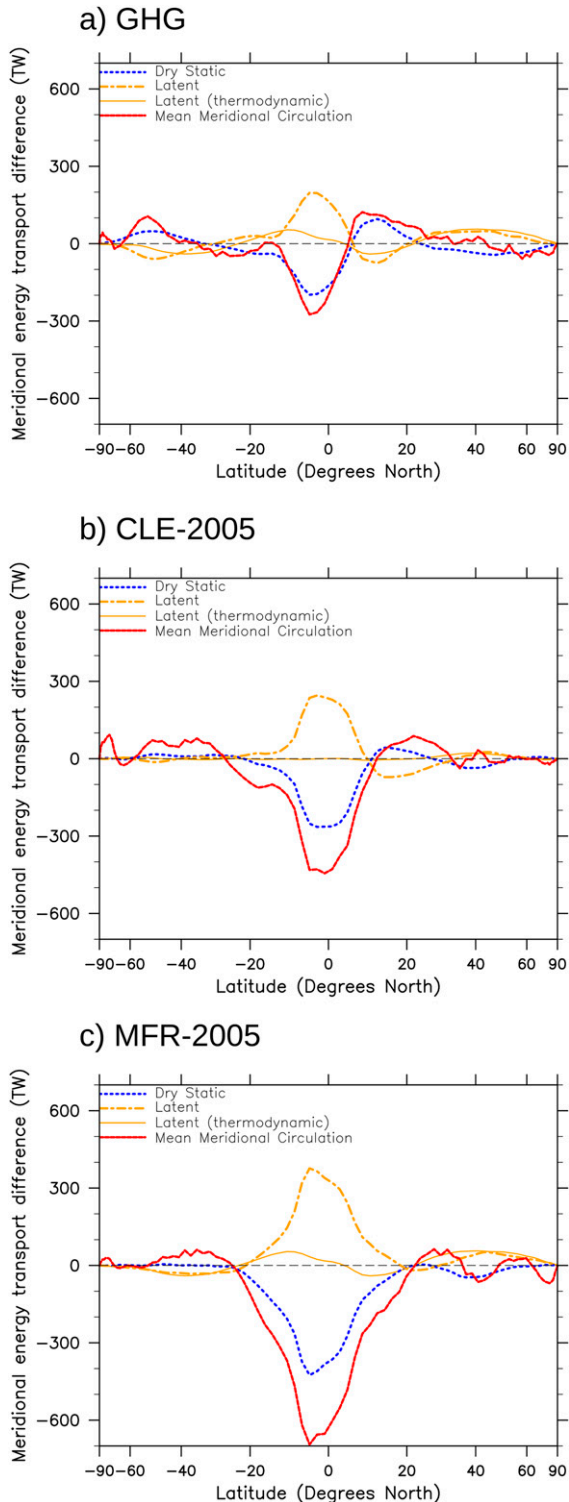


FIG. 7. Atmospheric meridional heat transport changes. Mean 2025–49 $F_{DS}(\phi)$, $F_{Latent}(\phi)$, and $F_{Merid}(\phi)$ change in (a) GHG, (b) CLE-2005, and (c) MFR-2005 cases. The thin yellow lines in (a)–(c) represent the approximate $F_{Latent}^{Therm}(\phi)$ estimated by the scaling in Clausius–Clapeyron relation, about 7% increase in water vapor per 1-K warming. The x axis scales latitude as $\sin\phi$ to display the relative area between parallels.

time-averaged energy budget equation for the climate system reads

$$\Delta \frac{\partial \overline{O(y)}}{\partial t} + \Delta \frac{\partial \overline{[F_A(y) + F_O(y)]}}{\partial y} = \Delta \overline{Q^{TOA}(y)}, \quad (10)$$

where Δ is the difference between a pair of simulations, $O(y)$ is the column-integrated, area-averaged, and zonally integrated oceanic energy content per unit length (J m^{-1}), $Q^{TOA}(y)$ is the area-averaged zonally integrated net downward flux at the TOA (W m^{-1}), and $y = a\phi$. To obtain a meridional energy transport compensation between $\Delta F_A(y)$ and $\Delta F_O(y)$ at a given latitude ϕ , then $\int_{-a\pi/2}^{a\phi} \Delta \{ \partial [F_A(y) + F_O(y)] / \partial y \} dy$ must be equal to zero. The three terms in Eq. (10) for GHG, CLE-2005, and MFR-2005 cases are shown in Fig. S2. No scenario shows perfect conditions for Bjerknes compensation, that is $\Delta \partial O(y) / \partial t = \Delta Q^{TOA}(y)$ at all latitudes. Nevertheless, MFR-2005 shows a larger net TOA energy flux than ocean heat uptake in most of the NH (Fig. S2c), while the SH oceans gain energy without significant changes in the net TOA energy flux in that hemisphere. These conditions lead to a clear noncompensating system that transports energy from the NH to the SH in both the ocean and atmosphere (Fig. 8c). In contrast to MFR-2005, the difference between ocean heat uptake and net TOA energy fluxes in both GHG and CLE-2005 cases are not large at a hemispheric scale (Figs. S2a,b), leading to a system with higher Bjerknes compensation (Figs. 8a,b). The oceanic energy transport change in MFR-2005 has the largest reduction ($\sim -4.0\%$ between 25° and 50°N) close to latitudes with maximum TOA energy gain (Figs. 2d and 8c), which indicates that the northward transport of heat in the ocean is weakened as a response to the strong aerosol emission reductions. This behavior of the oceanic heat transport is not observed in CLE-2005, which has a smaller surface warming than MFR-2005.

The change in total horizontal energy entering the Arctic cap in the GHG case is small (~ 0 TW at 70°N) resulting from the compensating atmosphere and ocean contributions, the ocean term being positive and the atmosphere term negative (Fig. 8a). In contrast, MFR-2005 yields a net substantial increase in horizontal energy entering the Arctic cap (~ 20 TW at 70°N), driven by atmospheric energy in the form of latent heat, without any atmospheric dry static and oceanic compensation (Figs. 7c and 8c). A part of the larger amplification of Arctic warming in MFR-2005 than in the GHG case (Table 3) could be explained by this difference. In addition to contributing to a local amplification of the warming, the excess in horizontal convergence of water vapor in the Arctic region drives a larger increase in

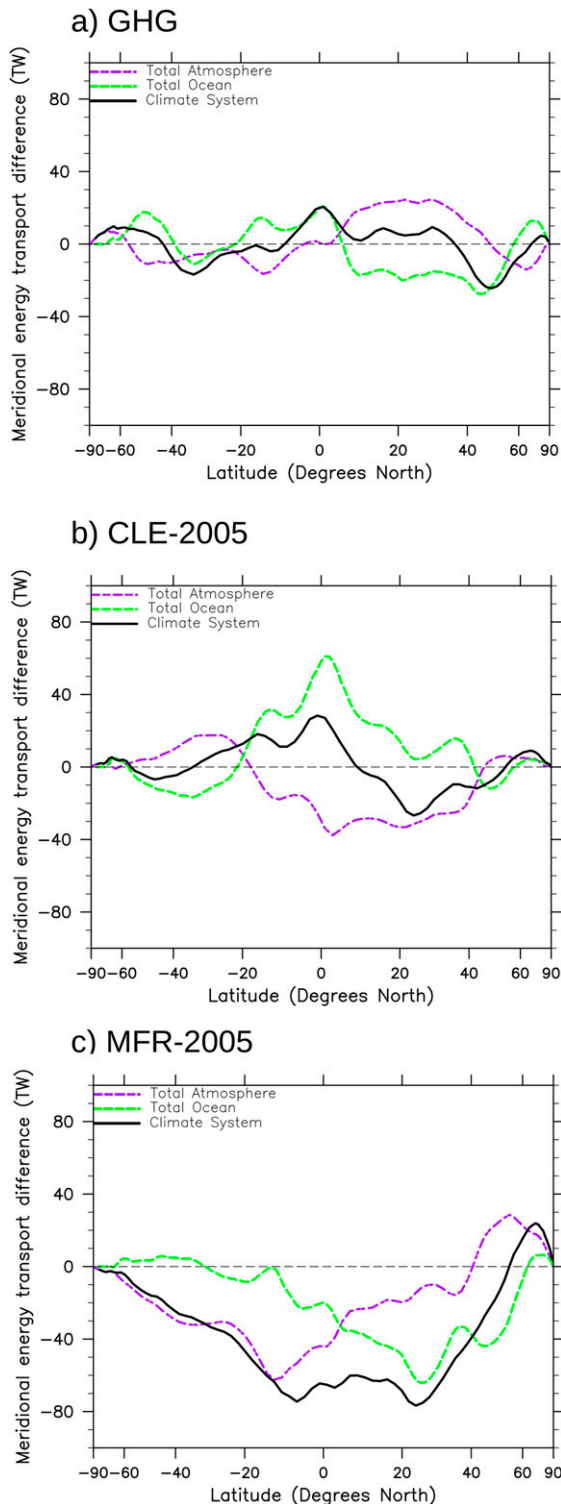


FIG. 8. Meridional heat transport changes in the climate system. Mean 2025–49 $F_O(\phi)$, $F_A(\phi)$, and $F_{\text{Sys}}(\phi)$ in (a) GHG, (b) CLE-2005, and (c) MFR-2005 cases. The x axis scales latitude as $\sin\phi$ to display the relative area between parallels.

precipitation north of 65°N in MFR-2005 than in the GHG case (Table 3).

4. Summary and conclusions

Using the climate model called NorESM1 we have studied the climate response to two future aerosol emission scenarios that include changes in black carbon, organic carbon, and sulfate aerosol emissions from fossil fuels. We have performed simulations to compare the distinctive climate effects of increasing greenhouse gas concentrations with that of changing aerosol emissions. The model results suggest that several important climate parameters, such as tropical precipitation, Asian monsoon circulation, and Arctic temperature, are particularly sensitive to aerosol emission changes, especially those occurring at midlatitudes in the Northern Hemisphere.

The model scenario where greenhouse gas concentrations follow RCP4.5 and aerosol emissions are fixed at the 2005 level (RCP4.5_2005) gives a global temperature increase of 0.60 K in 2025–49 compared to 2001–10. From the 0.60 K, about 0.35 K of the warming is caused by the increase in greenhouse gases between 2005 and 2050 and the remaining 0.25 K of warming is caused by a delayed response of the system to previous changes in greenhouse gas concentrations. The Arctic temperature increase is predicted to be considerably larger, 1.84 K since 2001–10. About 0.90 K of the Arctic warming is a delayed response and the remaining 0.94 K can be attributed to the changes in greenhouse gas concentrations between 2005 and 2050. The net radiative flux change is similar between the two hemispheres yielding a small (~ 20 TW) meridional energy transport change at the equator. The meridional atmospheric energy transport change is negative north of 50°N and to a large extent compensated by ocean energy transport changes.

If aerosol emissions follow a current legislation emissions (CLE) scenario (i.e., a modest change in aerosol emissions) and greenhouse gas concentrations follow the RCP4.5 emission scenario (RCP4.5_CLE), the temperature change between 2001–10 and 2025–49 is about the same as in RCP4.5_2005; that is, the aerosol reductions have a small impact on global average surface temperature (+0.03 K). However, the simulated slight warming of the Northern Hemisphere (+0.07 K) and slight cooling of the Southern Hemisphere (-0.02 K) induces a northward shift in the mean position of the ITCZ and a southward anomaly in the meridional atmospheric energy transport between 20°S and 50°N . As for the greenhouse gas-induced atmospheric energy transport changes, the ocean generally compensates for the atmospheric heat transport anomalies in RCP4.5_CLE.

Aerosol emission reductions of up to 80% by 2050 in the maximum technically feasible reduction (MFR) scenario (RCP4.5_MFR) cause an additional warming of 0.26 K (global) and 0.84 K (Arctic) compared to RCP4.5_2005 by 2025–49. There is a stronger northward shift in the mean position of the ITCZ compared to RCP4.5_2005 and the southward anomaly in the atmospheric energy transport south of 50°N is also substantially larger. In addition, the tropical ocean heat transport displays a southward anomaly. The TOA radiative flux changes at NH midlatitudes are large, and the change in energy uptake of the ocean is not confined to the same latitudes, leading to a net southward anomaly in ocean energy transport for the whole system south of 50°N and a net northward energy transport anomaly north of 50°N. At the same time, the atmosphere also displays a northward positive energy transport anomaly from 40°N and northward, which could be one of the reasons why the Arctic amplification is stronger.

The surface temperature response to the MFR scenario emissions has to be taken with caution, because air quality policies would also affect emissions and chemistry of methane, nitrogen oxides (NO_x), volatile organic compounds, and tropospheric ozone. These effects are not taken into account in this study and would most likely cause a cooling effect in the MFR scenario reducing the net warming. According to [Stohl et al. \(2015\)](#), methane emissions mitigation in NorESM1 could offset about 50% of the warming between 2005 and 2050 caused by the aerosol emissions reductions in the MFR scenario, but many of the climate effects caused by differential forcing of hemispheres, such as tropical precipitation changes or amplified Arctic warming, may still persist. Despite the adverse climate implications, the implementation of the policies leading to the MFR scenario would be highly beneficial to public health by avoiding premature deaths in highly populated regions where most of the particulate matter reductions would take place.

The changes in aerosol emissions following both CLE and MFR scenarios lead to an increase in precipitation in the northern tropics and a reduction in the southern tropics. The contribution to tropical precipitation changes in the Northern Hemisphere from increased greenhouse gas concentrations appears to be lower than the contribution from large aerosol emissions reductions. In addition to the zonally averaged increase in precipitation in the northern tropics, the modeled monsoon circulation in Asia is enhanced in the scenario with strong aerosol emission reductions (MFR scenario), causing an increase in East Asian and Southeast Asian rainfall and a decrease over the Arabian Peninsula.

We acknowledge that our findings are based on one single model and that this model has lower sensitivity to

overall changes in anthropogenic aerosol emissions than other state-of-the-art climate models with similar complexity in terms of aerosol–cloud–climate interactions ([Baker et al. 2015](#)). For this reason, and also because of the immediate policy relevance of the results, we encourage the community to perform similar studies.

Acknowledgments. Anthropogenic emission scenarios for air pollutants were provided by IIASA supported by the EU FP7 projects ECLIPSE (282688) and PEGASOS (265148). The research leading to these results has received funding from the Nordic Centres of Excellence CRAICC and eSTICC, Swedish Environmental Protection Agency project SCAC, European FP7 Integrated projects PEGASOS (265148) and ACCESS, European Research Council Grant ATMOGAIN (278277), and the Research Council of Norway through the EVA project (Grant 229771). The Swedish National Supercomputing Centre and NordStore (Project ns2345k) are acknowledged for computational resources for running and storing part of the simulations. The other part of the simulations and storage were performed on resources provided by UNINETT Sigma2—the National Infrastructure for High Performance Computing and Data Storage in Norway, projects NN2345k and NS2345K. We thank three anonymous reviewers for their valuable comments.

REFERENCES

- Abdul-Razzak, H., and S. J. Ghan, 2000: A parameterization of aerosol activation: 2. Multiple aerosol types. *J. Geophys. Res.*, **105**, 6837–6844, doi:10.1029/1999JD901161.
- Acosta Navarro, J. C., and Coauthors, 2016: Amplification of Arctic warming by past air pollution reductions in Europe. *Nat. Geosci.*, **9**, 277–281, doi:10.1038/ngeo2673.
- Baker, L. H., W. J. Collins, D. J. L. Olivié, R. Cherian, O. Hodnebrog, G. Myhre, and J. Quaas, 2015: Climate responses to anthropogenic emissions of short-lived climate pollutants. *Atmos. Chem. Phys.*, **15**, 8201–8216, doi:10.5194/acp-15-8201-2015.
- Bellouin, N., J. Rae, A. Jones, C. Johnson, J. Haywood, and O. Boucher, 2011: Aerosol forcing in the Climate Model Intercomparison Project (CMIP5) simulations by HadGEM2-ES and the role of ammonium nitrate. *J. Geophys. Res.*, **116**, D20206, doi:10.1029/2011JD016074.
- Bentsen, M., and Coauthors, 2013: The Norwegian Earth System Model, NorESM1-M—Part 1: Description and basic evaluation of the physical climate. *Geosci. Model Dev.*, **6**, 687–720, doi:10.5194/gmd-6-687-2013.
- Bjerknes, J., 1964: Atlantic air–sea interaction. *Advances in Geophysics*, Vol. 10, Elsevier, 1–82, doi:10.1016/S0065-2687(08)60005-9.
- Boer, G. J., and B. Yu, 2003: Dynamical aspects of climate sensitivity. *Geophys. Res. Lett.*, **30**, 1135, doi:10.1029/2002GL016549.
- Boucher, O., and Coauthors, 2013: Clouds and aerosols. *Climate Change 2013: The Physical Science Basis*, T. F. Stocker et al., Eds., Cambridge University Press, 571–657.
- Fasullo, J. T., and K. E. Trenberth, 2008a: The annual cycle of the energy budget. Part I: Global mean and land–ocean exchanges. *J. Climate*, **21**, 2297–2312, doi:10.1175/2007JCLI1935.1.

- , and —, 2008b: The annual cycle of the energy budget. Part II: Meridional structures and poleward transports. *J. Climate*, **21**, 2313–2325, doi:10.1175/2007JCLI1936.1.
- Hansen, J., R. Ruedy, M. Sato, and K. Lo, 2010: Global surface temperature change. *Rev. Geophys.*, **48**, RG4004, doi:10.1029/2010RG000345.
- Held, I. M., and B. J. Soden, 2006: Robust responses of the hydrological cycle to global warming. *J. Climate*, **19**, 5686–5699, doi:10.1175/JCLI3990.1.
- Hill, S. A., Y. Ming, and I. M. Held, 2015: Mechanisms of forced tropical meridional energy flux change. *J. Climate*, **28**, 1725–1742, doi:10.1175/JCLI-D-14-00165.1.
- Hwang, Y.-T., D. M. Frierson, and S. M. Kang, 2013: Anthropogenic sulfate aerosol and the southward shift of tropical precipitation in the late 20th century. *Geophys. Res. Lett.*, **40**, 2845–2850, doi:10.1002/grl.50502.
- Iversen, T., and Coauthors, 2013: The Norwegian Earth System Model, NorESM1-M—Part 2: Climate response and scenario projections. *Geosci. Model Dev.*, **6**, 389–415, doi:10.5194/gmd-6-389-2013.
- Kang, S. M., I. M. Held, D. M. Frierson, and M. Zhao, 2008: The response of the ITCZ to extratropical thermal forcing: Idealized slab-ocean experiments with a GCM. *J. Climate*, **21**, 3521–3532, doi:10.1175/2007JCLI2146.1.
- Kirkevåg, A., T. Iversen, J. E. Kristjánsson, Ø. Seland, and J. B. Debernard, 2008: On the additivity of climate response to anthropogenic aerosols and CO₂, and the enhancement of future global warming by carbonaceous aerosols. *Tellus*, **60A**, 513–527, doi:10.1111/j.1600-0870.2008.00308.x.
- , and Coauthors, 2013: Aerosol–climate interactions in the Norwegian Earth System Model—NorESM1-M. *Geosci. Model Dev.*, **6**, 207–244, doi:10.5194/gmd-6-207-2013.
- Klimont, Z., K. Kupiainen, C. Heyes, P. Purohit, J. Cofala, P. Rafaj, J. Borcken-Kleefeld, and W. Schoepp, 2016: Global anthropogenic emissions of particulate matter including black carbon. *Atmos. Chem. Phys. Discuss.*, doi:10.5194/acp-2016-880, in press.
- Kristjánsson, J., T. Iversen, A. Kirkevåg, Ø. Seland, and J. Debernard, 2005: Response of the climate system to aerosol direct and indirect forcing: Role of cloud feedbacks. *J. Geophys. Res.*, **110**, D24206, doi:10.1029/2005JD006299.
- Lamarque, J.-F., and Coauthors, 2010: Historical (1850–2000) gridded anthropogenic and biomass burning emissions of reactive gases and aerosols: Methodology and application. *Atmos. Chem. Phys.*, **10**, 7017–7039, doi:10.5194/acp-10-7017-2010.
- Lewinschal, A., A. M. Ekman, and H. Körnich, 2013: The role of precipitation in aerosol-induced changes in Northern Hemisphere wintertime stationary waves. *Climate Dyn.*, **41**, 647–661, doi:10.1007/s00382-012-1622-7.
- Ming, Y., and V. Ramaswamy, 2011: A model investigation of aerosol-induced changes in tropical circulation. *J. Climate*, **24**, 5125–5133, doi:10.1175/2011JCLI4108.1.
- Najafi, M. R., F. W. Zwiers, and N. P. Gillett, 2015: Attribution of Arctic temperature change to greenhouse-gas and aerosol influences. *Nat. Climate Change*, **5**, 246–249, doi:10.1038/nclimate2524.
- Palmer, T. N., 1999: A nonlinear dynamical perspective on climate prediction. *J. Climate*, **12**, 575–591, doi:10.1175/1520-0442(1999)012<0575:ANDPOC>2.0.CO;2.
- Pausata, F. S. R., M. Gaetani, G. Messori, S. Kloster, and F. J. Dentener, 2015: The role of aerosol in altering North Atlantic atmospheric circulation in winter and its impact on air quality. *Atmos. Chem. Phys.*, **15**, 1725–1743, doi:10.5194/acp-15-1725-2015.
- Ridley, H. E., and Coauthors, 2015: Aerosol forcing of the position of the intertropical convergence zone since AD 1550. *Nat. Geosci.*, **8**, 195–200, doi:10.1038/ngeo2353.
- Rotstayn, L. D., and U. Lohmann, 2002: Tropical rainfall trends and the indirect aerosol effect. *J. Climate*, **15**, 2103–2116, doi:10.1175/1520-0442(2002)015<2103:TRTATI>2.0.CO;2.
- Seo, J., S. M. Kang, and D. M. W. Frierson, 2014: Sensitivity of intertropical convergence zone movement to the latitudinal position of thermal forcing. *J. Climate*, **27**, 3035–3042, doi:10.1175/JCLI-D-13-00691.1.
- Shindell, D., and G. Faluvegi, 2009: Climate response to regional radiative forcing during the twentieth century. *Nat. Geosci.*, **2**, 294–300, doi:10.1038/ngeo473.
- Smith, S. J., J. van Ardenne, Z. Klimont, R. J. Andres, A. Volke, and S. Delgado Arias, 2011: Anthropogenic sulfur dioxide emissions: 1850–2005. *Atmos. Chem. Phys.*, **11**, 1101–1116, doi:10.5194/acp-11-1101-2011.
- Stern, D. I., and R. K. Kaufmann, 1999: Econometric analysis of global climate change. *Environ. Modell. Softw.*, **14**, 597–605, doi:10.1016/S1364-8152(98)00094-2.
- Stohl, A., and Coauthors, 2015: Evaluating the climate and air quality impacts of short-lived pollutants. *Atmos. Chem. Phys.*, **15**, 10 529–10 566, doi:10.5194/acp-15-10529-2015.
- Taylor, K. E., R. J. Stouffer, and G. A. Meehl, 2012: An overview of CMIP5 and the experiment design. *Bull. Amer. Meteor. Soc.*, **93**, 485–498, doi:10.1175/BAMS-D-11-00094.1.
- Trenberth, K. E., 1997: Using atmospheric budgets as a constraint on surface fluxes. *J. Climate*, **10**, 2796–2809, doi:10.1175/1520-0442(1997)010<2796:UABAAC>2.0.CO;2.
- , and D. P. Stepaniak, 2003: Covariability of components of poleward atmospheric energy transports on seasonal and interannual timescales. *J. Climate*, **16**, 3691–3705, doi:10.1175/1520-0442(2003)016<3691:COCOPA>2.0.CO;2.
- Wang, H., S.-P. Xie, and Q. Liu, 2016: Comparison of climate response to anthropogenic aerosol versus greenhouse gas forcing: Distinct patterns. *J. Climate*, **29**, 5175–5188, doi:10.1175/JCLI-D-16-0106.1.
- Westervelt, D. M., L. W. Horowitz, V. Naik, J.-C. Golaz, and D. L. Mauzerall, 2015: Radiative forcing and climate response to projected 21st century aerosol decreases. *Atmos. Chem. Phys.*, **15**, 12 681–12 703, doi:10.5194/acp-15-12681-2015.
- Xie, S.-P., B. Lu, and B. Xiang, 2013: Similar spatial patterns of climate responses to aerosol and greenhouse gas changes. *Nat. Geosci.*, **6**, 828–832, doi:10.1038/ngeo1931.
- Yang, Q., C. M. Bitz, and S. J. Doherty, 2014: Offsetting effects of aerosols on Arctic and global climate in the late 20th century. *Atmos. Chem. Phys.*, **14**, 3969–3975, doi:10.5194/acp-14-3969-2014.